Aalto University

OPEN ACCESS

This is an electronic reprint of the original article.
This reprint may differ from the original in pagination and typographic detail.

Liu, Yi; Wang, Jincheng; Cai, Wayne; Carlson, Blair E.; Lian, Junhe; Min, Junying

A thermo-metallurgical-mechanical model for microstructure evolution in laser-assisted robotic roller forming of ultrahigh strength martensitic steel

Published in:
Journal of Materials Research and Technology

DOI:
10.1016/j.jmrt.2023.05.228

Published: 01/07/2023

Document Version
Publisher's PDF, also known as Version of record

Published under the following license:
CC BY-NC-ND

Please cite the original version:
Liu, Y., Wang, J., Cai, W., Carlson, B. E., Lian, J., & Min, J. (2023). A thermo-metallurgical-mechanical model for microstructure evolution in laser-assisted robotic roller forming of ultrahigh strength martensitic steel. *Journal of Materials Research and Technology*, *25*, 451-464. https://doi.org/10.1016/j.jmrt.2023.05.228

This material is protected by copyright and other intellectual property rights, and duplication or sale of all or part of any of the repository collections is not permitted, except that material may be duplicated by you for your research use or educational purposes in electronic or print form. You must obtain permission for any other use. Electronic or print copies may not be offered, whether for sale or otherwise to anyone who is not an authorised user.

Available online at www.sciencedirect.com

jmr&t Journal of Materials Research and Technology

journal homepage: www.elsevier.com/locate/jmrt

A thermo-metallurgical-mechanical model for microstructure evolution in laser-assisted robotic roller forming of ultrahigh strength martensitic steel

Yi Liu [a], Jincheng Wang [a], Wayne Cai [b], Blair E. Carlson [b], Junhe Lian [c], Junying Min [a,*]

[a] School of Mechanical Engineering, Tongji University, Shanghai 201804, China
[b] Manufacturing System Research Laboratory, General Motors Global Research & Development, Warren, MI 48092, USA
[c] Department of Mechanical Engineering, Aalto University, Espoo 02150, Finland

ARTICLE INFO

Article history:
Received 20 January 2023
Accepted 25 May 2023
Available online 29 May 2023

Keywords:
Laser-assisted forming
Thermo-metallurgical-mechanical model
Phase transformation
Microstructure evolution
Heat source model

ABSTRACT

Laser-assisted robotic roller forming (LRRF) apparatus and process were developed to bend a plate to form a straight channel for ultrahigh strength steel MS1300. Since the thermal processing during the roller forming impacts the microstructure and mechanical behavior of the steel, an integrated thermo-metallurgical-mechanical finite element simulation considering the heat source, phase transformation and material constitutive models was established. A rectangular laser source was devised to homogenize the temperature around the bending corner and a new surface heat source model was proposed and validated. The phase transformation model accounting for the austenitization process, austenite decomposition and tempering was embedded in the finite element model through self-developed user subroutines. The predicted microstructure evolution and the phase distribution were consistent with experimental microstructure characterization. More specifically, it is found that tempering dominates at the inner layer of the bend, resulting in two different phases, i.e., the original and tempered martensitic phases after the LRRF process. The outer layer of the bend, however, goes through austenitization, quenching, and tempering processes, resulting in a combination of fresh martensite, a small amount of tempered martensite and retained austenite phases.

© 2023 The Authors. Published by Elsevier B.V. This is an open access article under the CC BY-NC-ND license (http://creativecommons.org/licenses/by-nc-nd/4.0/).

1. Introduction

Laser-assisted forming process has drawn increased attention due to its high flexibility and efficiency. The coupling of temperature, microstructure and deformation confounds the ability to understand the intrinsic mechanisms of the process through experiments. The combination of numerical modeling and experimental observation has become an effective and preferable approach to identify the complex

* Corresponding author.
E-mail address: junying.min@tongji.edu.cn (J. Min).

https://doi.org/10.1016/j.jmrt.2023.05.228

2238-7854/© 2023 The Authors. Published by Elsevier B.V. This is an open access article under the CC BY-NC-ND license (http://creativecommons.org/licenses/by-nc-nd/4.0/).

behavior of materials at elevated temperatures. There are numerous works on thermo-mechanical modeling of laser-assisted forming process. For example, Kant et al. [1] utilized a 3D nonlinear thermo-mechanical model to understand the bending mechanism and forming characteristics, e.g. distortions and springback in laser-assisted bending of M1A alloy; Guo et al. [2] analyzed the strain changes in laser-assisted four-point bending of aluminum alloy by FEA; Gisario et al. [3] adopted FE simulation to calculate the temperature and displacement in laser-assisted bending of titanium alloy and concluded that small bending radii could be obtained with higher laser power and more forming passes. The above work studied deformation behavior of materials at elevated temperature; however, the microstructure evolution was generally neglected. Thermo-metallurgical-mechanical modeling of laser-assisted forming processes was rarely reported albeit being studied for hot stamping and laser welding. For instance, Bok et al. [4] developed a thermo-metallurgical-mechanical model to account for the effect of boron addition and austenite deformation on transformation behavior during hot stamping of a boron steel and found that the final strength and residual stress distribution were significantly influenced by the austenite deformation. Krishna et al. [5] analyzed the residual stresses induced by phase transformation during laser beam welding of a low alloy steel through comparison of a thermo-mechanical model and a thermo-metallurgical-mechanical model. Tan et al. [6] declared that the tensile stresses were decreased and compressive residual stresses were increased when considering the solid-state phase transformation in modeling selective laser melting of titanium alloy. Most of the studies on thermo-metallurgical-mechanical modeling were performed to predict residual stresses after stamping or welding. However, extensions to the analysis of phase transformation or microstructure distribution in laser-assisted forming processes with more complicated thermal passes are seldom discussed, although this is of great significance to understand the mechanical properties of final formed components.

Thermo-metallurgical-mechanical FEA includes three key modeling elements, i.e., the heat transfer, phase transformation and mechanistic behavior of materials. The heat source model is the first key element since the thermal input has a significant influence on the phase transformation as well as deformation. Various heat source models have been put forward to better describe power density distribution during laser-based manufacturing. The most commonly used heat source model is the double ellipsoid volumetric heat source proposed by Goldak et al. [7], which has been proved to be very effective for predicting temperature fields in welding simulation [8]. In addition, many other heat source models have been put forward to better describe the heat flux distribution for specific applications. For example, the double-ellipsoidal heat source was extended to a double-ellipsoidal-conical heat source to simulate the temperature field in electron beam welding, narrow groove gas-tungsten-arc welding [9] and hybrid laser-arc welding [10]. Yadaiah and Bag [11] used an egg-configuration heat source in gas tungsten arc welding and diode laser welding simulation and found the maximum deviation between the experimental weld pool size and that from FE simulation was within 10%. Rong et al. [12] proposed a peak index increment-double cone heat source model to represent the heat flux in laser penetration welding, based on the experimental weld geometry. Li et al. [13] combined Gaussian distributed disc heat source with an exponential volume heat source to describe the energy input associated with the extreme high-speed laser material deposition. Overall, the above-mentioned heat source models are volumetric heat source; however, surface heat source models are generally preferred in laser forming or laser-assisted forming since melting is avoided in these processes and the heat applied in the thickness direction of the sheet can be neglected. Although there are some commonly used surface heat source models, such as Gaussian surface heat source, the accurate prediction of temperature field in laser forming or laser-assisted forming is still limited due to the lack of appropriate heat source model for some particular laser heating situations. In addition to the heat source, the phase transformation behavior is also extremely important for predicting the microstructure distribution. At present, different phase transformation kinetics for calculating the phase fractions are implanted into finite element based software, among which, the Johnson–Mehl–Avrami–Kolmogorov (JMAK) equation [14–16] and the Koistinen–Marburger (KM) relationship [17] are the most frequently-used transition models for diffusional phase transformation and non-diffusional phase transformation, respectively. Some modified transition kinetics are also adopted in welding simulation. For instance, the JMAK model was used to calculate the isothermal phase transformation and the Leblond model with an incremental function was applied to predict the phase transformation with an arbitrary thermal history [18]. The reaction kinetics proposed by Kirkaldy and Venugopalan and its modification was adopted by Sun et al. [19] and Chen et al. [20] to predict austenite decomposition during electron beam welding and submerged arc welding, respectively. Xia and Jin [21] also used the Leblond model to predict the solid-state transformation in welding simulation and the effect of thermal cycle and cooling rate were analyzed through the thermo-metallurgical FE model. The above researches in the field of welding mainly focus on the austenite decomposition behavior, i.e. from austenite to ferrite, pearlite, bainite and martensite; however, the peak temperature for laser-assisted forming is normally below the melting temperature, sometimes even below the austenitization temperature. Materials with an initial microstructure of fully martensite (e.g. martensitic steel) or partial martensite (e.g. dual-phase steel, quenching and portioning steel) may suffer from tempering within this temperature range. Therefore, accurate characterization of tempering effect is vital for predicting microstructure evolution, whereas, the research considering the tempering effect in the thermo-metallurgical-mechanical model is still deficient. Mukherjee et al. [22] proposed an analytical method to calculate the hardness of tempered martensite at non-isothermal tempering conditions. Zhou et al. [23] performed experimental and analytical investigations on the tempering kinetics of a hot-worked die steel and the relationship between the tempering parameters and hardness of steels was established. Sun et al. [24] found that martensite, which was produced during the first welding pass, was tempered during multi-pass welding; a JMAK type equation was then applied to describe the tempering kinetics in the FE model and the results showed that the microstructure and microhardness were consistent with the experiments. The mechanical part of the thermo-metallurgical-mechanical analysis of welding focused on the effects of thermal expansion, volume change due to phase transformation and transformation induced plasticity behavior, etc … on the residual stress of the welded joints [25]. While for laser-assisted forming, the plastic deformation due to the direct contact between metal sheet and tools plays a major role in the levels of stress and strain. Furthermore, the plastic deformation has an impact on the heat flux distribution and as a consequence, the microstructure distribution after laser-assisted forming is also affected.

Laser-assisted robotic roller forming (LRRF) is a new approach to bend high strength steel sheets without fracture that overcomes issues common to conventional roll forming and laser-assisted forming. Previous research conducted by the authors has proved that LRRF process has the ability to form ultrahigh strength steels to a near 90° channels with sharp bending radius and springback angle smaller than 1° [26]. A thermo-mechanical FE model was established to reconstruct the temperature field during LRRF, which was further applied to analyze the microstructure distribution at the cross-section of the bend. However, the former thermo-mechanical model was not capable of predicting microstructure evolution during LRRF process directly. In this research, a new heat source model and the phase transformation kinetics were imported into the Abaqus software by means of user subroutines. Afterwards a thermo-metallurgical-mechanical FE model was established and solved by Abaqus to predict the temperature, microstructure and deformation in LRRF process. The FE model was further validated through the temperature field captured by thermal camera. The microstructure and microhardness distribution and the microstructure evolution during LRRF are finally discussed based on the thermo-metallurgical-mechanical model.

2. Laser-assisted robotic roller forming

MS1300 steel sheets, with a thickness of 1.0 mm, were bent on a lab-scaled LRRF platform. The schematic of LRRF process is illustrated in Fig. 1 and the lab-scaled LRRF platform can be found from a previous publication [27]. The steel sheets with a dimension of 250 mm × 60 mm were clamped on the fixture

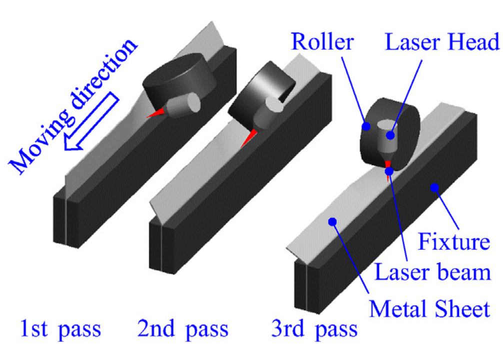

Fig. 1 – An illustration of LRRF process.

and then bent through three-passes sequential flanging by the combination of laser heating and roller contact. The laser head and roller were driven synchronously at a translational velocity of 0.03 m/s by an industrial robot (Kuka KR600), controlled by numerical programing. The laser beam preceded the roller at an offset of 25 mm to realize preheating prior to plastic deformation. A continuous wave fiber laser with a laser power of 1000W was applied. A rectangular laser source was adopted to ensure a more uniform temperature distribution at the bending corner since a laser beam with the commonly used small spot size would have too great a focused power density and thus degrade the sheet metal surface. The spot size of the laser beam was 4 mm × 2 mm. It should be noted that the laser spot size on the metal sheet varies with the inclination angle, which is detailed in Sec. 3.1. The cylindrical roller having a diameter of 50 mm and a height of 25 mm was fabricated from tool steel.

3. Thermo-metallurgical-mechanical model

A coupled thermo-metallurgical-mechanical model was established and solved in Abaqus Standard to account for the temperature field, microstructure evolution and plastic deformation during the simulated LRRF process. The temperature field has a significant influence on both the microstructure field and stress/strain field. The major factors, i.e. temperature induced transformation and thermal expansion are considered in the thermo-metallurgical-mechanical model. In addition to the temperature history, the plastic deformation also has an influence on the phase transition from retained austenite to martensite; whereas, the strain-induced martensitic transformation effect is not considered in this model based on the fact that the retained austenite fraction is negligible in martensitic steel. The modeling procedure and framework considering the coupled thermo-metallurgical-mechanical behavior during LRRF process is summarized in Fig. 2. The general settings, e.g. geometrical model, mesh, constraints, material constitutive model, are firstly built by Abaqus CAE. A new surface heat source model is established to describe the heat flux distribution of the laser beam and to reconstruct the temperature field during LRRF, and the heat source model is implemented into Abaqus by user subroutine DFLUX. The phase transformation model, accounting for the austenitizing behavior, austenite decomposition, and tempering effect is linked to the FE model through user subroutine USDFLD. Note that some parameters, such as phase fraction, microhardness value, are not variables in Abaqus's default outputs; therefore, these parameters are termed as solution dependent variables (SDVs). As a result, microstructure and microhardness distribution can be exported at each increment to the Abaqus output database file as field outputs and history outputs. These SDVs can be called in the subsequent increments. The user subroutine SDVINI is applied to define the initial value of the SDVs, which is only called by Abaqus at the first solving increment.

The geometrical dimension, as presented in Fig. 3, is simplified according to the experiments mentioned in Sec. 2; the lengths of the metal sheet and the fixture are 100 mm which is 250 mm in the experiments and the width of the

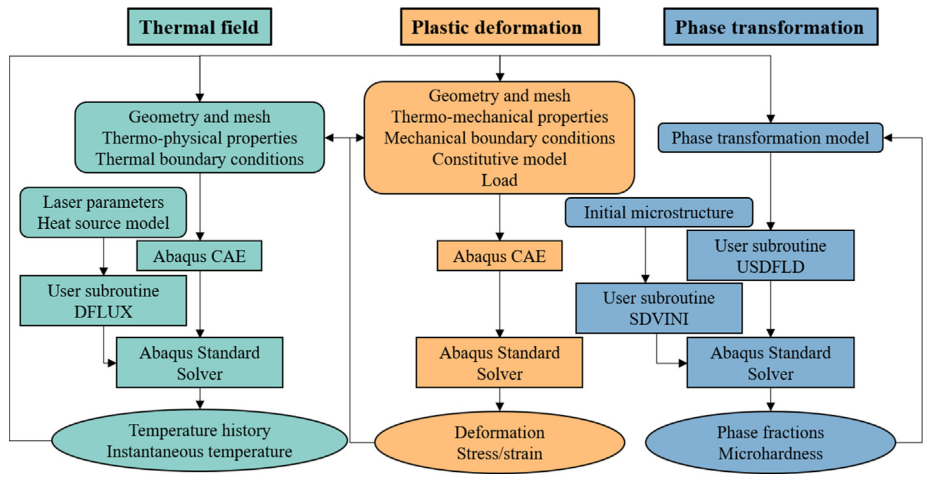

Fig. 2 – Framework of the coupled thermo-metallurgical-mechanical model using Abaqus software.

metal sheet in the FE model is 40 mm; the simplification is adopted for the purpose of reducing computation time. The fixture and the forming roller are defined as rigid bodies with a rigid body reference point. The translational and rotational motion of the rigid body can be defined on the reference point, which is normally the centroid of the rigid body. The fixture is restricted by six degrees of freedom. The fixture and roller are meshed with 4-node shell elements and the mesh size is 1 mm except that the corner of the fixture is refined with 5 elements. The metal sheet is meshed with 8-node hexahedron solid elements. The length of the metal sheet is meshed with a uniform element size of 0.5 mm and four elements are assigned through the thickness direction. Inhomogeneous mesh sizes are used along the width direction; the mesh sizes at the clamping area and the flange vary from 4 mm to 0.5 mm, and the bending corner has a refined mesh size of 0.2 mm. As a result, the smallest mesh size at the laser heating zone and also the bending corner is 0.5 mm × 0.2 mm × 0.25 mm. There are a total of 40,400 elements in the FE model.

The thermophysical properties for the MS1300 steel, including density (ρ), thermal conductivity (k), specific heat (c), thermal expansion coefficient (α), are calculated using JMatPro software according to the chemical composition (refer to Table 1) from Liu et al. [28] and the results are presented in Fig. 4.

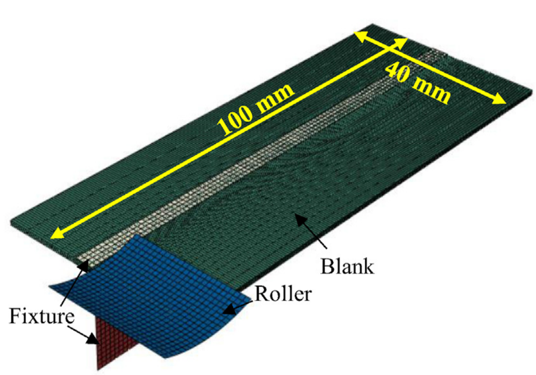

Fig. 3 – Assembly and mesh of LRRF.

The heat transfer analysis during LRRF process contains thermal conduction, thermal convection and thermal radiation. The heat transfers due to thermal convection (q_{con}) and thermal radiation (q_{rad}) between the high-temperature metal sheet and the surroundings follow Newton's law of cooling and the Stefan-Boltzmann law, respectively:

$$q_{con} = h\,(T - T_0) \tag{1a}$$

$$q_{rad} = \sigma\varepsilon \cdot \left(T^4 - T_0^4\right) \tag{1b}$$

here h is the convection heat transfer coefficient, and a constant value of 5 W/(m^2·K) is assumed for natural convection. T is the instantaneous temperature of the metal sheet. T_0 is the ambient temperature (set to 25 °C). σ is the Stefan-Boltzmann constant (5.67 × 10^{-8} W·m^{-2}·K^{-4}) and ε is the emissivity.

The time intervals between the first forming pass and second forming pass and that of the second forming pass and third forming pass are 26 s and 31 s, respectively, which are identical to the experiments. And an additional 600 s is adopted after the last forming pass so that the blank can be cooled to room temperature.

3.1. *Heat source model*

In the field of laser-based manufacturing, for example, laser welding, laser cutting, etc., the laser beam energy is generally assumed to follow a Gaussian distribution. However, centralized laser energy is sometimes unwanted to avoid melting or even vaporization in some situations, such as laser-assisted forming and laser surface heat treatment. Thus, in this study an integrating mirror is used for homogenization of the focus intensity. A combined Gaussian-uniform heat source model is proposed in this work based on the experimental temperature distribution of the rectangular laser spot as illustrated in Fig. 5. A local Cartesian coordinates is introduced at the center of the rectangular laser spot having the dimension of $a \times b$; the laser irradiated surface is defined as

Table 1 – The chemical composition of as-received MS1300 steels (wt%).

C	Mn	Si	Cr	Mo	B	Al	Ti	Cu	Nb	P	Fe
0.21	1.5	0.75	0.375	0.375	0.0075	0.0075	0.056	0.15	0.056	0.015	Bal.

the xy-plane and the laser scanning direction is defined as the x-axis; the laser energy along the y-axis is uniform to guarantee larger heating area and the laser energy along the x-axis still follows Gaussian distribution. Therefore, the governing equation of the power intensity can be written as:

$$q(x,y) = q_0 \cdot exp\left(-\frac{x^2}{2\delta^2}\right) \; while \; -\frac{b}{2} \le y \le \frac{b}{2} \tag{2a}$$

where q_0 is power intensity at the center of the rectangular laser spot, δ is the standard deviation of the Gaussian function. Note that the total laser heat input follows:

$$\int_{-b/2}^{b/2}\int_{-\infty}^{+\infty} q(x,y)dxdy = \eta Q \tag{2b}$$

here Q is the laser power and η is the laser absorption rate of the workpiece. The standard deviation of the Gaussian function is set as Eq. (2c) which indicates that 99.74% of the laser energy is applied on the rectangular laser spot.

$$3\delta = \frac{a}{2} \tag{2c}$$

Combining Eqs. (2a)–(2c), The combined Gaussian-uniform heat source is eventually expressed as follows:

$$q(x,y) = \frac{6\eta Q}{\sqrt{2\pi}ab} \cdot exp\left(-\frac{18x^2}{a^2}\right) \; while \; -\frac{b}{2} \le y \le \frac{b}{2} \tag{3}$$

The laser spot size is relevant to the focused spot size, defocusing distance as well as the inclination angle between laser beam and metal sheet. The focused spot size is determined according to the laser head and there is no defocusing distance in this study to guarantee maximum heating efficiency. The inclination angle varies by different bending passes, as schematically presented in Fig. 6; therefore, the proposed heat source model is modified to Eq. (4) to account for the effect of inclination angle of the laser beam and bending angle of the flange:

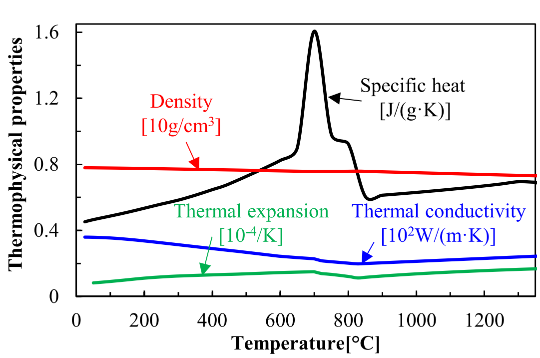

Fig. 4 – Thermophysical properties of MS1300 steel according to JMatPro.

$$q(x,y) = \frac{6\eta Q \cos\alpha \cos\gamma}{\sqrt{2\pi}ab} \cdot exp\left(-\frac{18x^2\cos^2_\gamma}{a^2}\right) \; while \; -\frac{b}{2\cos\alpha} \le y < 0 \tag{4a}$$

$$q(x,y) = \frac{6\eta Q \cos(\alpha-\beta)\cos\gamma}{\sqrt{2\pi}ab} \cdot exp\left(-\frac{18x^2\cos^2_\gamma}{a^2}\right) \; while \; 0 \le y \le \frac{b\cos\beta}{2\cos(\alpha-\beta)} \tag{4b}$$

where α, β denote the inclination angle between the laser beam and xz-plane and yz-plane, respectively, and γ indicates the bending angle of the metal sheet. Model parameters such as inclination angle, laser power, bend angle in this new heat source model are explicit according to the experimental setup. Therefore, the only unclear parameter, i.e. laser absorption rate of the metal sheet, can be easily calibrated by the peak temperature of the laser heating and consequently a value of 0.39 is obtained in this study.

3.2. *Phase transformation model*

The MS1300 steel metal sheet undergoes austenitizing, austenite decomposition and tempering during the LRRF process. Microstructure evolution is highly dependent on the instantaneous temperature, holding time at a specific temperature range and sometimes the cooling rate. The phase fractions are updated by each time increment in LRRF simulation following the procedure in Fig. 7, till the end of the last forming pass. In addition to the superheating or supercooling to activate the corresponding phase transitions, some other preconditions are also necessary for austenite decomposition. For instance, austenite is transformed to ferrite, pearlite and bainite only when the cooling rate is below the critical cooling rate (CCR) for martensite transformation.

The austenite transformation kinetics upon heating can be simplified to a linear relationship [29,30]. In this study, a modified equation is used to account for the austenite transformation from ferrite, pearlite, bainite, martensite and tempered martensite:

$$f_A = \frac{T - A_{C1}}{A_{C3} - A_{C1}} \times \sum_{k=1}^{4} f_k \quad while \; A_{C1} \le T \le A_{C3} \tag{5}$$

f_k denotes the fraction of different microstructure, namely, k = 1,2,3,4 for ferrite and pearlite, bainite, martensite, and tempered martensite, respectively. T is instantaneous temperature; A_{C1} and A_{C3} are austenite start and finish temperatures, which are estimated to be 732 °C and 842 °C [31], respectively, for the given steel grade.

On cooling, the JMAK equation is adopted to describe the diffusional phase transformation from austenite to ferrite, pearlite, and bainite:

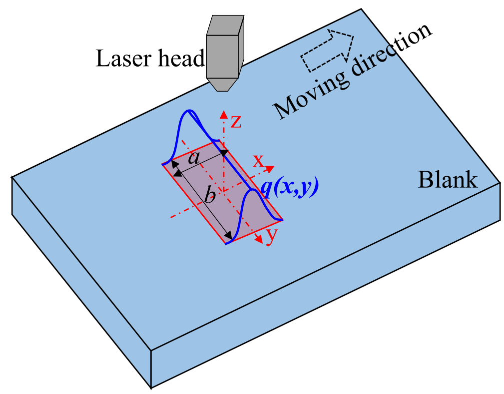

Fig. 5 – Schematic of the combined Gaussian-uniform heat source.

$$f_k = f_A\left(1 - e^{-\alpha t^{\beta}}\right) \tag{6}$$

α and β are material parameters, which can be obtained from the time-temperature-transformation (TTT) diagram using the following equation [32]:

$$\alpha = -\frac{\ln(0.99)}{t_{0.01}{}^{\beta}} \tag{7a}$$

$$\beta = \frac{\ln\frac{\ln 0.99}{\ln 0.01}}{\ln\frac{t_{0.01}}{t_{0.99}}} \tag{7b}$$

here, $t_{0.01}$ and $t_{0.99}$ denote the transformation start time and finish time, respectively, as can be seen in Fig. 8. Note that the phase fractions of 0.01 and 0.99 are regarded as the start and finish of ferrite, pearlite and bainite transformation in this study.

It should be noted that Eq. (6) is based on isothermal transformation. To account for the influence of critical cooling rate for the start of transformation in a situation of continuous cooling, the rule of additivity proposed by Lusk and Jou [33] is applied. The transformation is assumed to occur when the following equation is fulfilled:

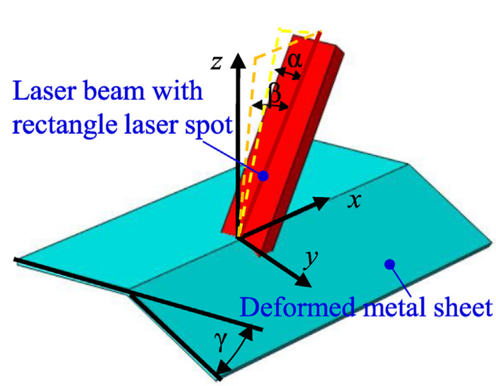

Fig. 6 – Laser spot varies by bending angle (γ) and inclination angle between laser and *xz*-plane (α)/yz-plane (β).

$$\sum_{i=1}^{j}\frac{\Delta t}{t_i} \geq 1 \tag{8}$$

where Δt is the time increment and t_i is the transformation start time on isothermal transformation at the temperature of the ith time increment.

In this study, ferrite and pearlite are simplified to one phase because of the low carbon content in MS1300 steel, namely, the phase transformation from austenite to ferrite and pearlite at the temperature range from A_{C1} to bainite start temperature (B_S), and phase transformation from austenite to bainite from B_S to martensite start temperature (M_S) are considered. B_S and M_S are 544 °C and 392 °C, respectively, according to the empirical equation [34] relating to the composition of the steel.

$$B_S(^{\circ}C) = 637 - 58C - 35Mn - 34Cr - 15Ni - 41Mo \tag{9a}$$

$$M_S(^{\circ}C) = 539 - 423C - 30.4Mn - 12.1Cr - 17.7Ni - 7.5Mo + 10Co - 7.5Si \tag{9b}$$

The parameters of diffusional phase formation are calculated according to the TTT diagram from JMatPro. Specifically, the parameter β is a constant: $\beta = 3.5$ for ferrite and pearlite transformation, and $\beta = 2$ for bainite transformation.

The transformation from austenite to martensite is regarded as non-diffusional phase transformation, which is determined by the K-M relationship:

$$f_M = f_A \cdot \left[1 - e^{-\delta(M_S - T)}\right] \quad \textit{while } T \leq M_S \tag{10}$$

where δ is the empirical coefficient, and a value of 0.011 is suggested for carbon steel and low alloy steel according to Krauss [35].

Tempering can be generally categorized into three stages [36]: The first stage involves the precipitation of very fine transition carbides in martensite crystals at temperatures between 100 °C and 200 °C. Transformation of retained austenite to ferrite and cementite occurs during the second stage, in the temperature range of 200 °C–300 °C. The third stage takes place between 300 °C and the A_{C1} temperature; in this stage, transition carbides and segregated carbon transform into cementite; recovery or recrystallization by the nucleation and growth of new grains takes place; and for highly alloyed steels, alloy carbide precipitation and secondary hardening takes effect.

The Vickers hardness of martensitic steel during tempering (H_S) can be quantified by the fraction of tempered martensite (f_{TM}) as follows:

$$H_S = f_{TM} \cdot H_{TM} + (1 - f_{TM}) \cdot H_M \tag{11a}$$

$$f_{TM} = \frac{H_M - H_S}{H_M - H_{TM}} \tag{11b}$$

where H_M and H_{TM} are the Vickers hardness of initial martensite and fully tempered martensite.

Tempering can be considered as a phase transformation controlled by diffusion; therefore, the tempering kinetics are also represented by the JMAK equation as Eq. (12):

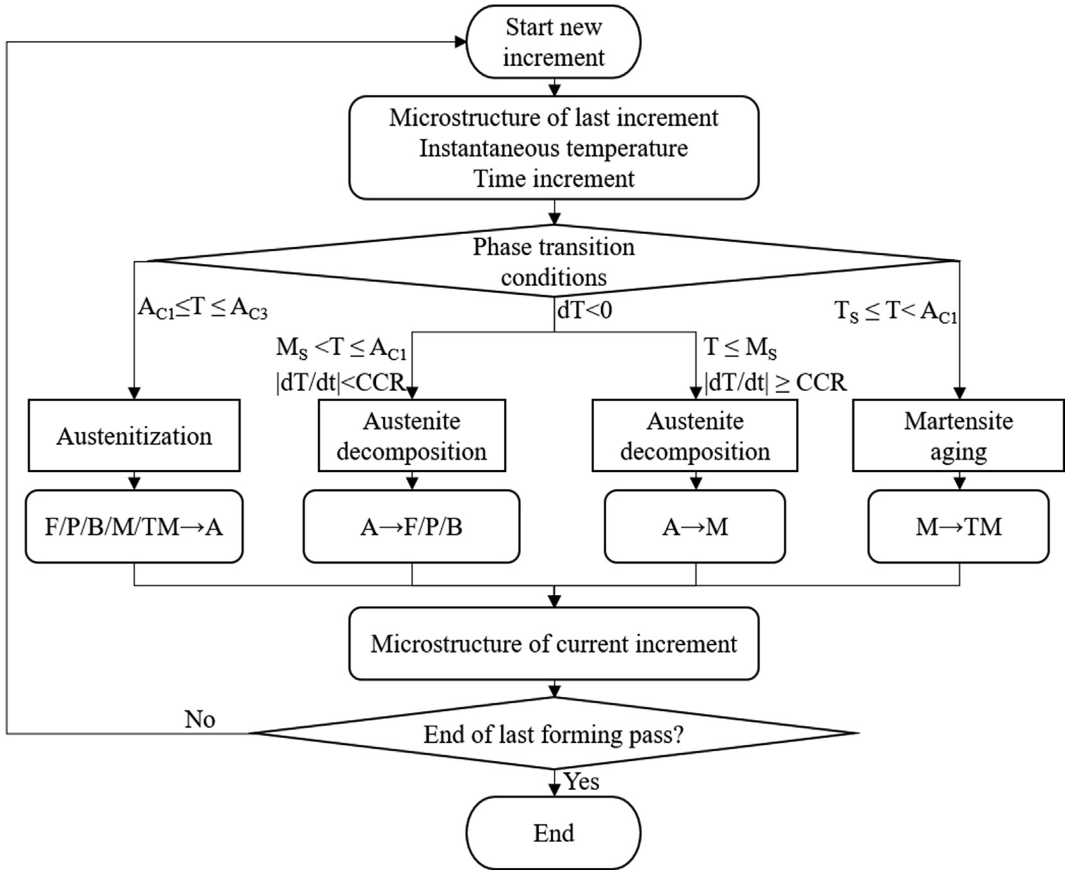

Fig. 7 – Procedure for calculating phase transformation during LRRF modeling (A_{C1}: austenite start temperature; A_{C3}: austenite finish temperature; T: instantaneous temperature; M_S: martensite start temperature; dT: Temperature variation; |dT/dt|: cooling rate; CCR: critical cooling rate for martensite transformation; T_S: tempering start temperature; A: austenite; F: ferrite; P: pearlite; B: bainite; M: martensite; TM: tempered martensite).

$$f_{TM} = f_M \cdot \left(1 - e^{-Dt^m}\right) \tag{12}$$

where t is tempering time and m is the Avrami exponent. D is related to temperature, which can be described as Eq. (13), according to the Arrhenius equation:

$$D = D_0 e^{-\frac{Q}{RT}} \tag{13}$$

where D_0 is the pre-exponential constant, Q is the activation energy for tempering, and R is the universal gas constant (equal to 8.314 $J \cdot mol^{-1} \cdot K^{-1}$).

Eq. (12) and Eq. (13) can be expressed in the natural logarithmic form:

$$\ln\ln\frac{f_M}{f_M - f_{TM}} = m \ln t + \ln D \tag{14a}$$

$$\ln D = \ln D_0 - \frac{Q}{RT} \tag{14b}$$

The slope and y-intercept of the plots of $\ln\ln\frac{f_M}{f_M - f_{TM}}$ vs. $\ln t$ can be used to determine the value of m and $\ln D$ at different temperatures. Similarly, the values of Q and D_0 can be obtained according to the plots of $\ln D$ and $1/T$.

In this study, the third tempering stage is considered due to the dramatic microstructure changes within this stage [36]. The Vickers hardness from JMatPro is introduced into Eq. (11b) to calculate the tempering ratio. The parameters of the tempering kinetics, summarized in Table 2, are subsequently obtained based upon Eqs. (14a) and (14b).

The microhardness of final microstructure is calculated by the rule of mixtures as follows:

$$H = f_A \cdot H_A + f_{F+P} \cdot H_{F+P} + f_B \cdot H_B + f_M \cdot H_M + f_{TM} \cdot H_{TM} \tag{15}$$

here f and H denote fraction and hardness, respectively and the subscript letters indicate the specific microstructure: austenite (A), ferrite and pearlite ($F+P$), bainite (B), martensite (M) and tempered martensite (TM).

The microhardness of initial martensite is 439.5 HV, which is a mean value of five experimental indentations measured by a hardness tester. The microhardness of the others is calculated by empirical formula according to Doane [37], in which the hardness of ferrite and pearlite, bainite, martensite can be calculated based on the chemical composition and cooling rate at 700 °C. The cooling rate at 700 °C after laser heating is ~1000 °C/s according to experiments and as a result,

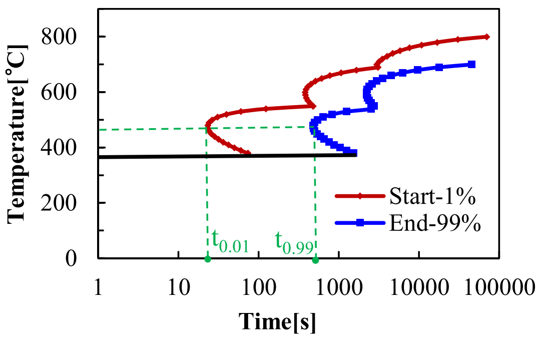

Fig. 8 – Material parameters according to the TTT diagram from JMatPro.

the microhardness values of ferrite and pearlite, bainite, martensite are calculated to be 171.1 HV, 316.5 HV and 506.7 HV, respectively. The microhardness of fully tempered martensite microstructure is set to be equivalent to that of ferrite and pearlite, and the microhardness of austenite is not considered given the relatively small amount and thus, the relatively small contribution to the total microhardness values compared with the other microstructures.

3.3. *MS1300 constitutive models*

An isotropic hardening constitutive model for the MS1300 steel sheet was used for mechanical simulation with Abaqus. Quasi-static uniaxial tensile tests with the aid of digital image correlation (DIC) system [38], refer to Fig. 9(a), were performed with a MTS universal tensile testing machine to obtain the flow curve of MS1300 steel at the following temperatures: 25 °C, 200 °C, 400 °C, 600 °C and 800 °C. Three samples were repeated at each temperature and the temperature-dependent Young's modulus and true stress vs. plastic strain curves are given in Fig. 9(b) and (c), respectively. It is found that the elongation is improved at elevated temperature, especially when the temperature exceeds 600 °C. Work hardening dominates in the temperature range of 25 °C–200 °C while softening is quite obvious at temperatures above 400 °C; the tensile testing results also provide inspiration for regulating the deformation temperature in LRRF.

4. Results and discussion

4.1. *Temperature field*

A dedicated platform was built to calibrate and validate the new surface heat source as presented in Fig. 10, since accurate temperature data during LRRF was difficult to capture experimentally. Laser irradiation with a laser power of 1000 W was imposed on a flat metal sheet and an inclination angle between the metal sheet and the laser beam was set to ~53°. Two thermal cameras were used to capture the spatio-temporal temperature fields of the irradiated surface and non-irradiated surface of the metal sheet during laser heating. Because an obvious temperature gradient exists between the irradiated surface and non-irradiated surface [28], two different thermal cameras were used. The top camera (Optris PI 08 M, #1 in Fig. 10) measured the temperature between 575 °C and 1900 °C while the bottom position camera (Optris PI 400, #2 in Fig. 10) had a temperature range of −20 °C–900 °C; both thermal cameras have a frame rate of 80 Hz to accurately record the temperature history. The emissivity value of the metal sheet during thermal imaging was calibrated with temperature measurements via thermocouples.

The new surface heat source model was compared with three other commonly used surface heat source models, i.e. the uniform heat source model, the Gaussian heat source model and the elliptical heat source model. The heat flux density of the above heat source models follows Eqs. (16a)–(16c). These four heat source models were imported into Abaqus to construct the temperature field and the parameters of these heat source models were calibrated by using experimentally measured peak temperatures. The isotherm profiles from experiments and FE model according to different heat source models are presented and compared in Fig. 11. It is obvious that the isotherm profiles based on the new heat source model proposed in this work exhibit a high degree of correlation with those captured by IR camera.

$$q(x,y) = \frac{\eta Q}{ab} \quad while \quad -\frac{a}{2} \le x \le \frac{a}{2}, -\frac{b}{2} \le y \le \frac{b}{2} \tag{16a}$$

$$q(x,y) = \frac{2\eta Q}{\pi b^2} \cdot exp\left(-\frac{2(x^2+y^2)}{b^2}\right) \tag{16b}$$

$$q(x,y) = \frac{8\eta Q}{\pi ab}\, exp\left(-\frac{8x^2}{a^2}\right) exp\left(-\frac{8y^2}{b^2}\right) \tag{16c}$$

Temperature data along the transversal direction, namely perpendicular to the laser scanning direction, were extracted on the irradiated and non-irradiated surface, refer to Fig. 12(a). It is found that the temperature on the irradiated surface agrees well with the experimental data, though minor errors exist between the predicted and experimental values on the non-irradiated surface (refer to Fig. 12(b)). Despite some small deviations, the FE model is quite reliable to predict the temperature distribution. The temperature history was also extracted from four points in Fig. 12(a) and the predicted temperature vs. time curves match well with the experiments, refer to Fig. 12(c), which also proves the accuracy of the thermal boundary conditions.

Table 2 – Parameters of tempering kinetics.

T (°C)	300	350	400	450	500	550	600	650	700
m	0.38	0.33	0.27	0.22	0.19	0.17	0.15	0.14	0.14
Q (kJ/mol)	49.38				D_0 (s^{-1})	530.86			

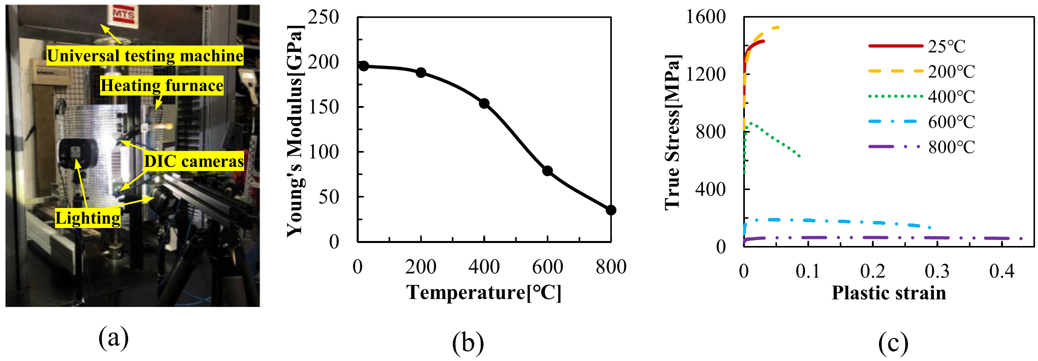

Fig. 9 – Uniaxial tensile tests: (a) tensile testing with DIC system; (b) temperature-dependent Young's modulus; (c) true stress vs. plastic strain curves of MS1300 steel.

Temperature fields at the irradiated surface and along the thickness direction during LRRF process are collected from the thermo-metallurgical-mechanical model, as presented in Fig. 13. It can be found that the temperature field, or the laser power density applied to the metal sheet is quite different for each pass although the same laser parameters are adopted, specifically, the temperature field during the first and third forming passes are almost symmetrical on the clamping and flange side while quite asymmetrical during the second forming pass. The metal sheet is not deformed or deformed slightly as the laser beam impinges on the sheet during the first forming pass. It should be noted that the inclination angle between the laser beam and both the clamping side and the flange are nearly identical resulting in a symmetrical temperature field during the first forming pass. However, the laser power density imposed on the clamping side and flange during the second forming pass is obviously different because of the deformed steel sheet, refer to Fig. 6, which leads to an asymmetrical temperature field. Although the laser inclination angle difference between the clamping side and flange still exists during the third forming pass, the laser beam is almost parallel to the clamping side, thus there is rarely laser power imposed on the clamping side, and the temperature field seems to be symmetrical because of heat conduction.

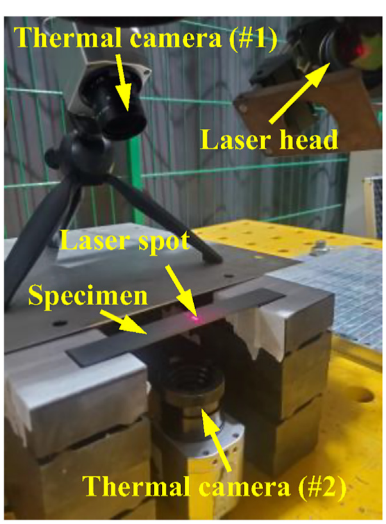

Fig. 10 – Experimental setup for calibration and validation of the heat source model.

Temperature history of two sampling points at the center of the bending corner (see Fig. 14(a)) are also extracted from both the irradiated surface and the non-irradiated surface. As can be observed in Fig. 14(b), temperature differences of 615 °C, 610 °C, and 697 °C exist between the irradiated surface and the non-irradiated surface for three continuous forming passes. Furthermore, it is also observed that these two sampling points undergoes various temperature cycles; the peak temperature on the irradiated surface is above austenitization temperature, while the peak temperature on the non-irradiated surface is always below the austenitization temperature. The asymmetrical temperature field between the clamping side and flange, the temperature difference between the irradiated and non-irradiated surfaces and repeated heating and cooling would all influence the microstructure evolution and distribution.

4.2. *Microstructure evolution*

FE simulation results predict no presence of ferrite, pearlite or bainite after LRRF processing, which is quite reasonable since the cooling rates in LRRF are much larger than the critical cooling rate for martensitic transformation. The predicted fractions of martensite, tempered martensite and retained austenite are depicted in Fig. 15. Note the sum of the fractions of martensite, tempered martensite and retained austenite is equal to 1. Obvious microstructure gradients can be observed around the heating area, and the asymmetric microstructural distribution is still notable due to the asymmetric laser power energy imposed on the clamping side and deformed flange. A small amount of retained austenite (2.6%) and tempered martensite (1.9%) appear at the outer layer of the bend and the remainder is martensite (95.5%). The retained austenite is beneficial to the toughness of the bend [39]. The microstructure at the inner layer of the bend after forming consists of ~67.8% martensite and ~32.2% tempered martensite. It is also interesting to note that the middle layer has a larger amount of tempered martensite (~41.8%) than the outer and inner layers, as the temperature at the middle layer is lower than

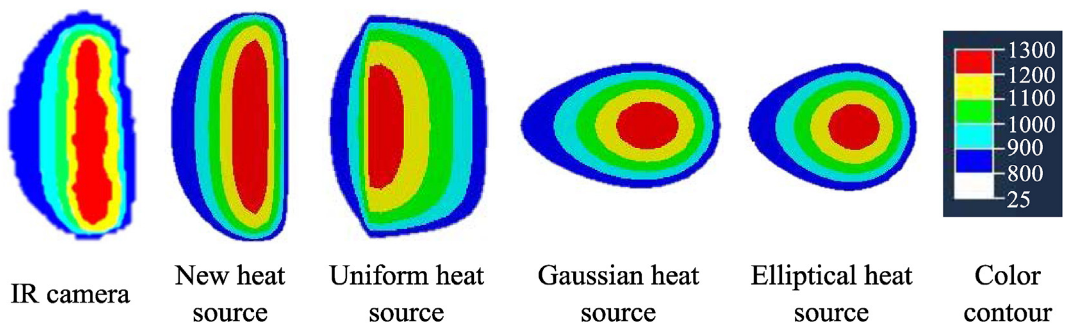

Fig. 11 – Effect of heat source model on temperature field of laser heating.

the austenitization temperature and its tempering effect is more pronounced than that of the inner layer. The tempered martensite is also conducive to improving the ductility and toughness of the bend [40].

The bending corner suffers from the most severe heat input, therefore, metallographic samples around the bending corner were prepared by cutting, mounting, grinding, polishing and etching. Metallographic images were then captured from four positions identified in Fig. 16(a), i.e. the base metal, the outer, middle and inner layers of the bend, by scanning electron microscope (SEM) at magnifications of 2000× and 5000×. The as-received material was a fully martensitic steel, according to Fig. 16(b). The outer layer of the bend exhibits a refined martensitic microstructure in contrast to the original martensite, indicating the formation of fresh martensite, refer to Fig. 16(c). A martensitic structure can be still observed within the middle layer, refer to Fig. 16(d), whereas a large amount of blocky microstructure composed of ferrite and carbide precipitates (tiny white particles at a magnification of 5000×) also appear in the grains, which suggests that tempered martensite was formed. It is worth mentioning that carbide precipitations can be rarely found since the steel has a low carbon contents (0.21%) and the material is just partially tempered with a relatively short duration of a few seconds. The inner layer (refer to Fig. 16(e)) also consists of martensite and tempered martensite. The experimental microstructure distribution is consistent with the numerically predicted results presented in Fig. 15.

Microhardness gradients are also noted as a result of the microstructure differences, as can be observed in Fig. 17(a). The predicted microhardness values were extracted from the outer, middle and inner layers. The microhardness values around the outer, middle and inner section of the sample were measured with an interval of 0.32 mm to validate the fraction of different phases, as can be observed in Fig. 17(b). The experimental microhardness values are generally consistent

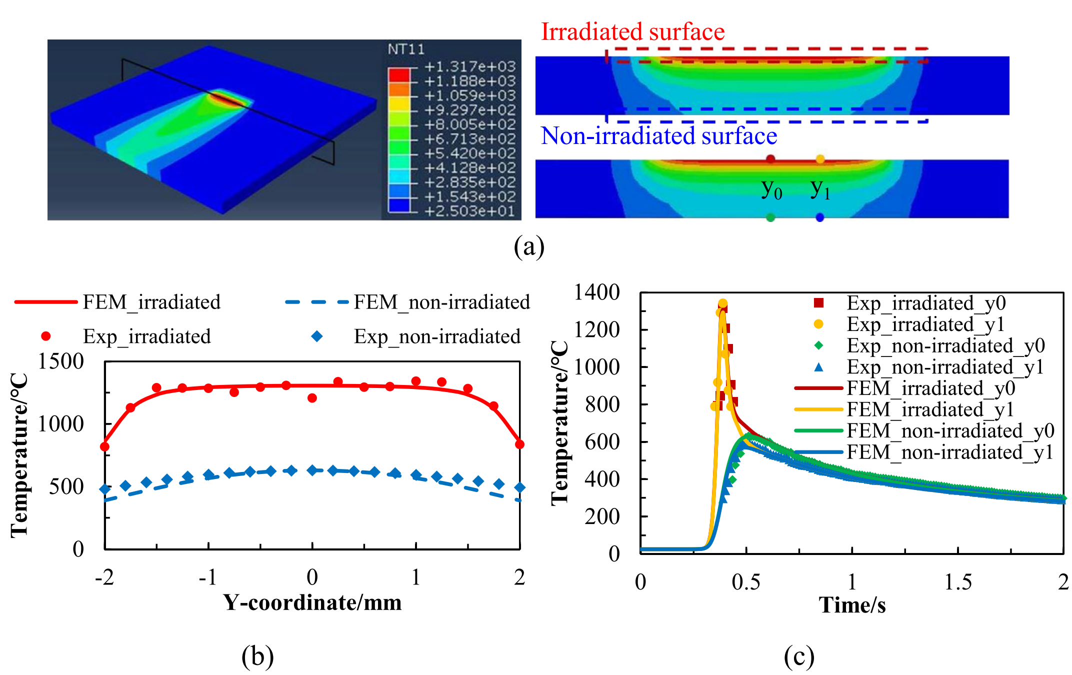

Fig. 12 – Validation of the heat source model: (a) the cross-section and position from which temperature data were extracted; (b) temperature distribution along the transversal direction; (c) temperature history of the four points in Fig. 12(a).

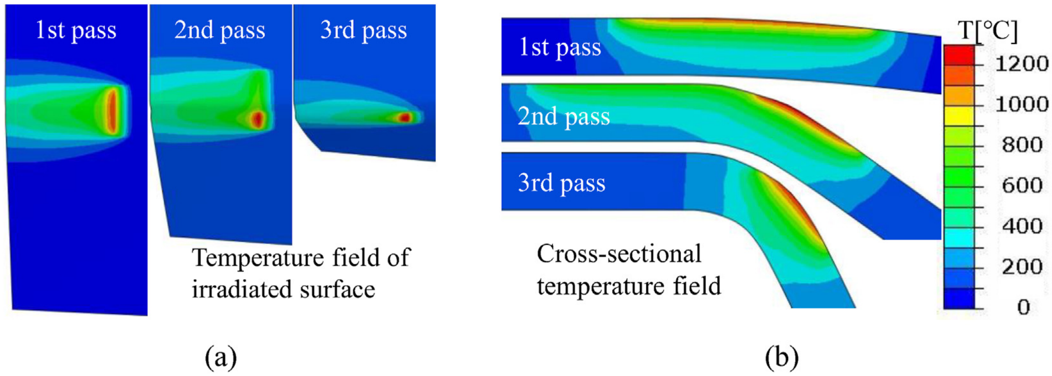

Fig. 13 – Temperature field during LRRF process, (a) temperature field of the irradiated surface, (b) temperature field along the thickness direction.

with the predicted profiles, although some discrepancies still exist. In addition to the phase compositions, the experimental microhardness at the bending corner can be also influenced by the work hardening effects due to plastic deformation, as well as the grain sizes changes due to recrystallization, while these two factors are not considered in the present model, and this is possibly responsible for the deviation between experiments and prediction. The microhardness at the outer layer follows a W-shaped profile while the microhardness profiles at the inner and middle layers are U-shaped. Both the simulated and experimental results indicate the obvious hardening zone at the outer layer of the bending corner, and softening zones at the middle and inner layers of the bending corner, as well as softening zone at the region very close to the laser-irradiated position of the outer layer. Although both the outer layer of the bending corner and the base metal are mainly composed of fully martensite, as shown in Figs. 15 and 16, the microhardness of the outer layer of the bending corner is larger than that of the base metal, and this can be explained by the fact that the hardness of the martensite is related to not only the chemical composition, but also the cooling rate of quenching. The higher cooling rate during LRRF, in contrast to conventional quenching approach, results in greater hardness values in the outer layer of the bend in comparison to the base metal. The simulation results also emphasize the significance of considering the tempering effect in modeling of laser-assisted forming. As the martensitic transformation leads to the hardening effect at the outer layer of the bending corner and there are no other softening phases, i.e. ferrite, pearlite and bainite due to fast cooling, the tempering effect is responsible for the softening zones at the bending corner.

The microstructure evolution of the two sampling points at the outer and inner layers of the bend as depicted in Fig. 14(a), are given in Fig. 18. Note that only the first forming pass is exemplarily provided here since the temperature history is similar for each forming pass. It can be found that the outer layer passed through austenitization, quenching and tempering in the first forming pass, while only tempering takes place at the inner layer of the bend. The outer layer is therefore composed of fresh martensite, tempered martensite and retained austenite after LRRF and the inner layer consists of original martensite and tempered martensite. It is also interesting to note that tempering occurred with two stages at the outer layer. Original martensite was firstly tempered during the heating stage and the newly-generated tempered martensite transformed into austenite shortly thereafter since the peak temperature exceeded the austenitization temperature. Afterwards, the fresh martensite was also tempered to a certain extent during the cooling stage. The tempering of original martensite is much more remarkable

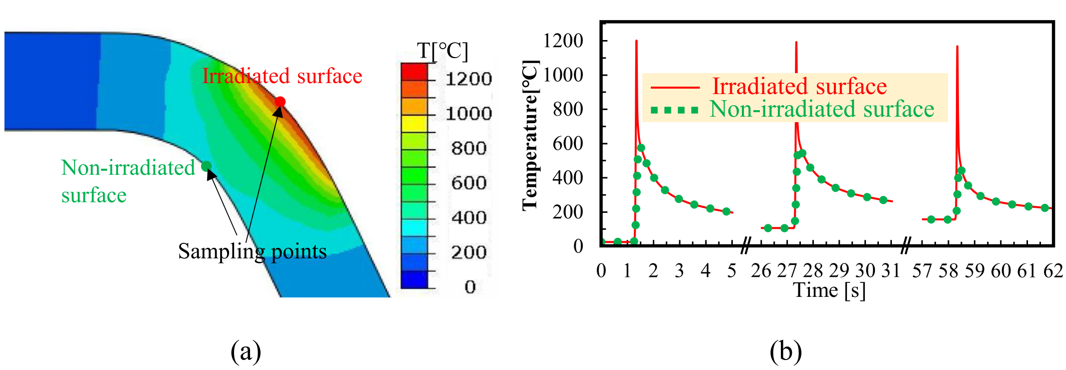

Fig. 14 – (a) Temperature gradients during LRRF, (b) temperature history of two sampling points from the irradiated surface and non-irradiated surface.

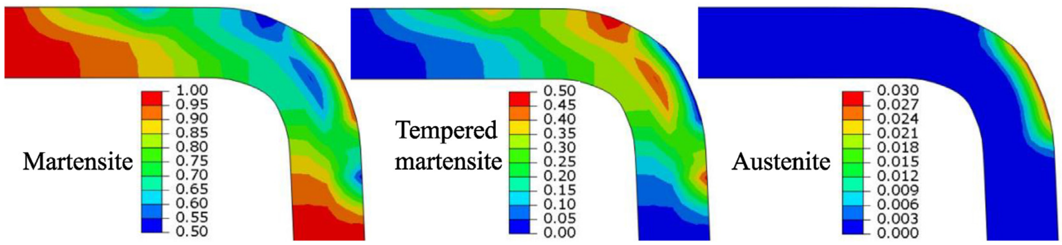

Fig. 15 – Fractions of various microstructure after LRRF.

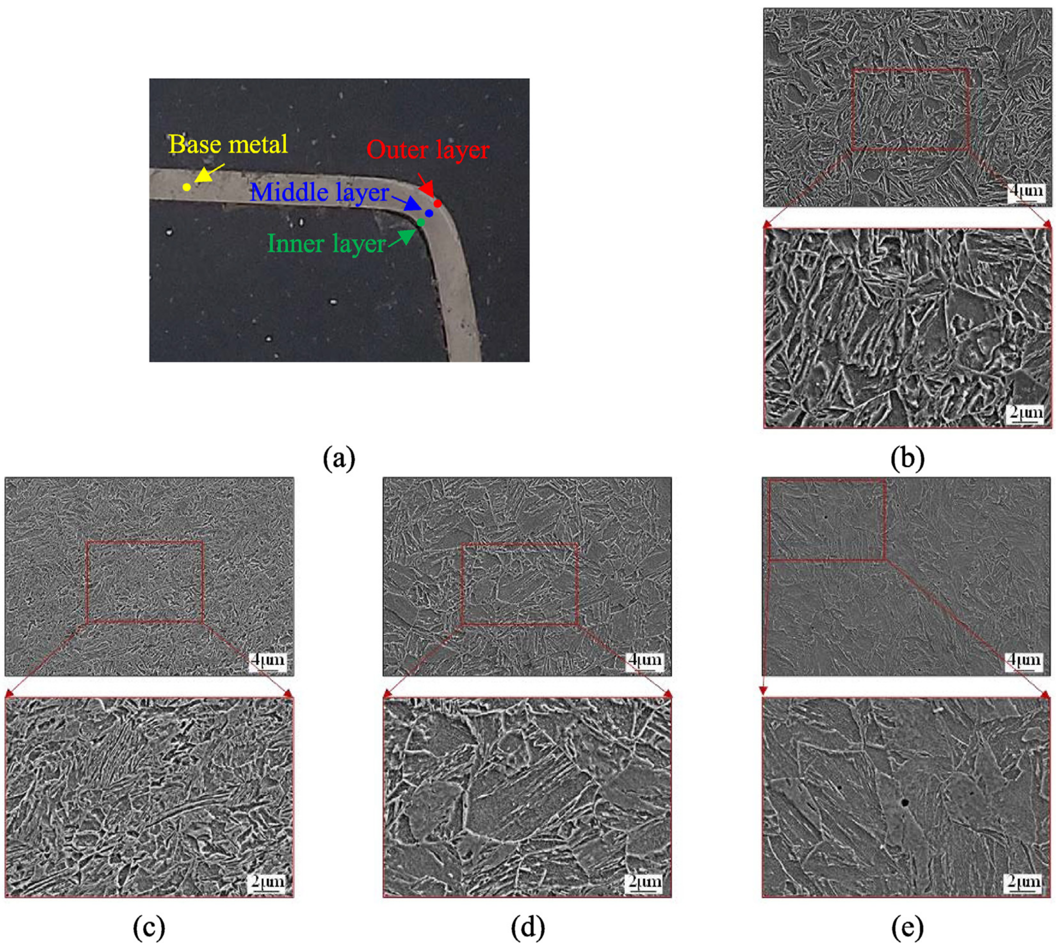

Fig. 16 – Metallographic images obtained by SEM, (a) sampling positions, (b) base metal, (c) outer layer, (d) middle layer, (e) inner layer.

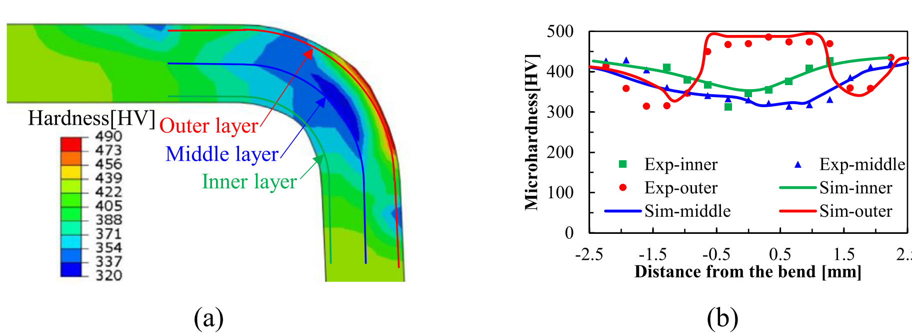

Fig. 17 – Comparison of the microhardness at the bending corner, (a) microhardness distribution according to the FE simulation, (b) microhardness values from the experiments and simulation.

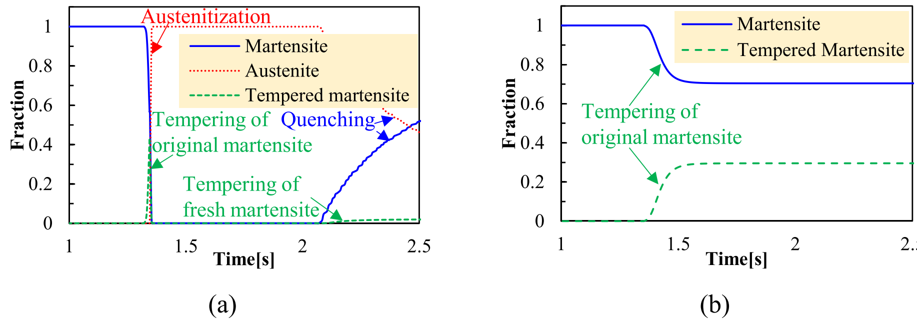

Fig. 18 – Microstructure evolution of the (a) outer and (b) inner sections of the bending corner.

than that of fresh martensite due to various martensite fractions at two stages. The initial fully martensitic structure is responsible for the more significant tempering effect at the first tempering stage. Whereas fresh martensite is formed gradually from reverted austenite with the decrease of temperature, and the fraction of fresh martensite is relatively low at higher temperatures at which tempering is prone to take place, and tempering is less likely to occur at lower temperatures in spite of higher martensite fraction, leading to a very small amount of tempered martensite at the second tempering stage. The original martensite at the inner layer suffered from continuous tempering effect during both heating and cooling stages. The longer duration at the tempering temperature range results in a larger amount of tempered martensite at the inner layer. Unlike the tempered martensite transformed from fresh martensite at the outer layer, the tempered martensite at the inner layer results from the tempering effect of original martensite.

5. Conclusions

In this work, the LRRF process is developed using an advantageous rectangle shaped laser source. An integrated numerical model is successfully established through a newly-developed thermo-metallurgical-mechanical FE procedure to simulate the LRRF process. The FE simulation is validated in terms of temperature field, microstructure and microhardness profiles. The main conclusions are summarized as follows:

(1) The newly-proposed combined Gaussian-uniform surface heat source model considering the inclination angle of laser and bend profile successfully reproduces the temperature field of laser-assisted forming.
(2) Hardening effect at the outer layer due to the formation of fresh martensite and the softening effect with the transformation from martensite to tempered martensite are well predicted by the coupled thermo-metallurgical-mechanical model.
(3) The FEM indicates that the outer layer of a 1.0 mm thick MS1300 steel goes through tempering, austenitization and quenching during LRRF while the inner layer mainly undergoes tempering. The outer layer is thus composed of 95.5% fresh martensite, 2.6% retained austenite and 1.9% tempered martensite while the inner layer consists of 67.8% initial martensite and 32.2% tempered martensite.

The integrated thermo-metallurgical-mechanical finite element simulation procedure is expected to be further adaptable to other materials (such as DP and Q&P steels, or titanium alloys) and different manufacturing processes (such as welding and 3D printing). The extension to the more detailed mechanical analysis in laser-assisted forming is also expected with the advanced constitutive models to describe the complicated deformation behavior (e.g. ref. [41]), which is the scope of further research.

CRediT authorship contribution statement

Yi Liu: Methodology, Software, Formal analysis, Investigation, Writing – Original Draft; **Jincheng Wang:** Validation, Data Curation; **Wayne Cai:** Conceptualization, Supervision; **Blair E. Carlson:** Funding acquisition, Writing – Review & Editing; **Junhe Lian:** Writing – Review & Editing; **Junying Min:** Writing – Review & Editing, Supervision, Project administration; Funding acquisition.

Declaration of competing interest

The authors declare that they have no known competing financial interests or personal relationships that could have appeared to influence the work reported in this paper.

Acknowledgements

This research was supported by Science and Technology Commission of Shanghai Municipality (Grant number: 21170711200) and General Motors collaborative research project (GAC3599). Yi Liu would like to acknowledge Mr. Xian Zhang and Mr. Junpeng Qiu for their assistance in the experiments. Yi Liu is also grateful for the support from China Scholarship Council (Grant number: 202206260121).

REFERENCES

[1] Kant R, Gurung H, Sarma U, Joshi SH. Development and analysis of laser-assisted bending with moving pre-displacement load. Laser Eng 2021;49:21–47.

[2] Guo J, Li W, Wan M, Zhao Y, Li C. Design of an innovative laser-assisted four-point bending forming process for high-stiffened structure of aluminum alloy. Opt Laser Technol 2021;143:107313.

[3] Gisario A, Mehrpouya M, Venettacci S, Barletta M. Laser-assisted bending of Titanium Grade-2 sheets: experimental analysis and numerical simulation. Opt Laser Eng 2017;92:110–9.

[4] Bok H-H, Choi J, Barlat F, Suh DW, Lee M-G. Thermo-mechanical-metallurgical modeling for hot-press forming in consideration of the prior austenite deformation effect. Int J Plast 2014;58:154–83.

[5] Krishna Murthy KR, Akyel F, Reisgen U, Olschok S. Simulation of transient heat transfer and phase transformation in laser beam welding for low alloy steel and studying its influences on the welding residual stresses. J Adv Join Process 2022;5:100080.

[6] Tan P, Shen F, Li B, Zhou K. A thermo-metallurgical-mechanical model for selective laser melting of Ti6Al4V. Mater Des 2019;168:107642.

[7] Goldak J, Chakravarti A, Bibby M. A new finite element model for welding heat sources. Metall Trans B 1984;15B:299–305.

[8] Lou M, Cai W, Huang J, Wang H-P, Li Y, Carlson BE, et al. Simulation of laser brazing of sheet panels and parametric studies of thermally-induced distortion reduction. J Manuf Process 2020;60:1–10.

[9] Flint TF, Francis JA, Smith MC, Balakrishnan J. Extension of the double-ellipsoidal heat source model to narrow-groove and keyhole weld configurations. J Mater Process Technol 2017;246:123–35.

[10] Chen L, Mi G, Zhang X, Wang C. Numerical and experimental investigation on microstructure and residual stress of multi-pass hybrid laser-arc welded 316L steel. Mater Des 2019;168:107653.

[11] Yadaiah N, Bag S. Development of egg-configuration heat source model in numerical simulation of autogenous fusion welding process. Int J Therm Sci 2014;86:125–38.

[12] Rong Y, Mi G, Xu J, Huang Y, Wang C. Laser penetration welding of ship steel EH36: a new heat source and application to predict residual stress considering martensite phase transformation. Mar Struct 2018;61:256–67.

[13] Li T, Zhang L, Chen G, Pirch N, Schopphoven T, Gasser A, et al. A combined heat source model for the prediction of residual stress post extreme high-speed laser material deposition. J Manuf Process 2022;78:265–77.

[14] Johnson WA, Mehl RF. Reaction kinetics in processes of nucleation and growth. Trans AIME 1939;135:416–58.

[15] Avrami M. Kinetics of phase change. I General theory. J Chem Phys 1939;7:1103–12.

[16] Kolmogorov AN. On the statistical theory of crystallization of metals. Bull Acad Sci USSR Ser Math 1937;1:355–9.

[17] Koistinen DP, Marburger RE. A general equation prescribing the extent of the austenite-martensite transformation in pure iron-carbon alloys and plain carbon steels. Acta Metall 1959;7:59–60.

[18] Du Z, Sun X, Ng FL, Chew Y, Tan C, Bi G. Thermo-metallurgical simulation and performance evaluation of hybrid laser arc welding of chromium-molybdenum steel. Mater Des 2021;210:110029.

[19] Sun YL, Vasileiou AN, Pickering EJ, Collins J, Obasi G, Akrivos V, et al. Impact of weld restraint on the development of distortion and stress during the electron beam welding of a low-alloy steel subject to solid state phase transformation. Int J Mech Sci 2021;196:106244.

[20] Chen W, Xu L, Zhao L, Han Y, Jing H, Zhang Y, et al. Thermo-mechanical-metallurgical modeling and validation for ferritic steel weldments. J Constr Steel Res 2020;166:105948.

[21] Xia J, Jin H. Numerical modeling of coupling thermal–metallurgical transformation phenomena of structural steel in the welding process. Adv Eng Software 2018;115:66–74.

[22] Mukherjee M, Dutta C, Haldar A. Prediction of hardness of the tempered martensitic rim of TMT rebars. Mater Sci Eng, A. 2012;543:35–43.

[23] Zhou Q, Wu X, Shi N, Li J, Min N. Microstructure evolution and kinetic analysis of DM hot-work die steels during tempering. Mater Sci Eng, A. 2011;528:5696–700.

[24] Sun YL, Obasi G, Hamelin CJ, Vasileiou AN, Flint TF, Francis JA, et al. Characterisation and modelling of tempering during multi-pass welding. J Mater Process Technol 2019;270:118–31.

[25] Rong Y, Lei T, Xu J, Huang Y, Wang C. Residual stress modelling in laser welding marine steel EH36 considering a thermodynamics-based solid phase transformation. Int J Mech Sci 2018;146–147:180–90.

[26] Min J, Wang J, Lian J, Liu Y, Hou Z. Laser-assisted robotic roller forming of ultrahigh strength steel QP1180 with high precision. Materials 2023;16:1026.

[27] Liu Y, Min J, Lin J. Robotic roller forming process and strategies to eliminate geometrical defect of edge waves. Forming the Future. Cham: Springer; 2021. p. 479–91.

[28] Liu Y, Min J, Zhang J, Cai W, Carlson BE, Bobel AC, et al. Laser-assisted robotic roller forming of an ultrahigh strength martensitic steel. J Manuf Process 2022;82:192–202.

[29] Cheon J, Na S-J. Prediction of welding residual stress with real-time phase transformation by CFD thermal analysis. Int J Mech Sci 2017;131–132:37–51.

[30] Wang H, Woo W, Kim D-K, Em V, Lee SY. Effect of chemical dilution and the number of weld layers on residual stresses in a multi-pass low-transformation-temperature weld. Mater Des 2018;160:384–94.

[31] Kasatkin OG, Vinokur BB, Pilyushenko VL. Calculation models for determining the critical points of steel. Met Sci Heat Treat 1984;26:27–31.

[32] Kang S-H, Im Y-T. Three-dimensional finite-element analysis of the quenching process of plain-carbon steel. Metall Mater Trans A 2005;36A:2315–25.

[33] Lusk M, Jou HJ. On the rule of additivity in phase transformation kinetics. Metall Mater Trans A 1997;28A:287–91.

[34] Li MV, Niebuhr DV, Meekisho LL, Atteridge DG. A computational model for the prediction of steel hardenability. Metall Mater Trans B 1998;29B:661–72.

[35] Krauss G. Principles of heat treatment of steel. Materials Park, Ohio: ASM International; 1990.

[36] Krauss G. Tempering of martensite in carbon steels, Phase transformations in steels. Woodhead Publishing Limited; 2012.

[37] Doane DV. Application of hardenability concepts in heat treatment of steel. J Heat Treat 1979;1:5–30.

[38] Guo N, Hou Z, Wang W, Zhang X, Yang D, Min J, et al. Flow stress modeling of ultra-thin austenitic stainless steel for proton exchange membrane fuel cell incorporating strain rate, temperature, and grain size. J Mater Process Technol 2023. submitted for publication.

[39] Wang YQ, Duan RH, Hu J, Luo ZA, Ma ZY, Xie GM. Improvement in toughness and ductility of friction stir welded medium-Mn steel joint via post-welding annealing. J Mater Process Technol 2022;306:117621.

[40] Liu Y, Lin J, Min J, Ma Z, Wu B. Effect of deep cryogenic treatment on mechanical properties and microstructure of the tool steel CR7V for hot stamping. J Mater Eng Perform 2018;27:4382–91.

[41] Hou Y, Min J, El-Aty AA, Han HN, Lee M-G. A new anisotropic-asymmetric yield criterion covering wider stress states in sheet metal forming. Int J Plast 2023;166:103653.